Sensors and Materials, Vol. 12, No. 6 (2000) 327–351
MYU Tokyo

S & M 0413

Quantum Well Infrared Photodetector Research and Development at Jet Propulsion Laboratory

S. D. Gunapala, S. V. Bandara, J. K. Liu, E. M. Luong,
S. B. Rafol, J. M. Mumolo, D. Z. Ting, J. J. Bock,
M. E. Ressler, M. W. Werner, P. D. LeVan[1], R. Chehayeb[2],
C. A. Kukkonen[2], M. Levy[3], P. LeVan[3] and M. A. Fauci[4]

Jet Propulsion Laboratory, California Institute of Technology, Pasadena, CA 91109, USA
[1]Air Force Research Laboratory, Kirtland Air Force Base, NM 87117, USA
[2]QWIP Technologies, Altadena, CA 91001, USA
[3]University of Southern California Hospital, Los Angeles, CA 90027, USA
[4]OmniCorder Technologies, Inc., Stony Brook, NY 11790, USA

(Received July 25, 2000; accepted October 4, 2000)

***Key words*:** infrared detectors, long-wavelength infrared, multi quantum well, multi-color, focal plane arrays

One of the simplest device realizations of the classic particle-in-the-box problem of basic quantum mechanics is the quantum well infrared photodetector (QWIP). In this paper we discuss the effect of focal plane array nonuniformity on the performance, optimization of the detector design, material growth and processing that has culminated in the realization of large format, long-wavelength QWIP cameras, holding forth great promise for many applications in the 6–18 micron wavelength range in science, medicine, defense and industry. In addition, we present the recent developments in long-wavelength/very long-wavelength dualband QWIP imaging camera for various applications.

1. Introduction

The idea of using multi-quantum-well (MQW) structures to detect infrared radiation can be explained by using the basic principles of quantum mechanics. The quantum well is equivalent to the well known particle-in-a-box problem in quantum mechanics, which can be solved by the time independent Schrodinger equation. The solutions to this problem are the Eigen values that describe energy levels inside the quantum well in which the particle is allowed to exist. The positions of the energy levels are primarily determined by the quantum well dimensions (height and width). For infinitely high barriers and parabolic bands, the energy levels in the quantum well are given by[1]

$$E_j = \left(\frac{h^2\pi^2}{2m^* L_w^2} \right) j^2 , \tag{1}$$

where L_w is the width of the quantum well, m^* is the effective mass of the carrier in the quantum well, and j is an integer. Thus, the intersubband energy between the ground and the first excited state is

$$(E_2 - E_1) = (3h^2\pi^2 / 2m^* L_w^2) . \tag{2}$$

The quantum well infrared photodetectors (QWIPs) discussed in this article utilize the photoexcitation of an electron (hole) between the ground state and the first excited state in the conduction (valance) band quantum well (see Fig. 1). The quantum well structure is designed so that these photoexcited carriers can escape from the quantum well and be collected as photocurrent. In addition to larger intersubband oscillator strength, these detectors afford greater flexibility than extrinsically doped semiconductor infrared detec-

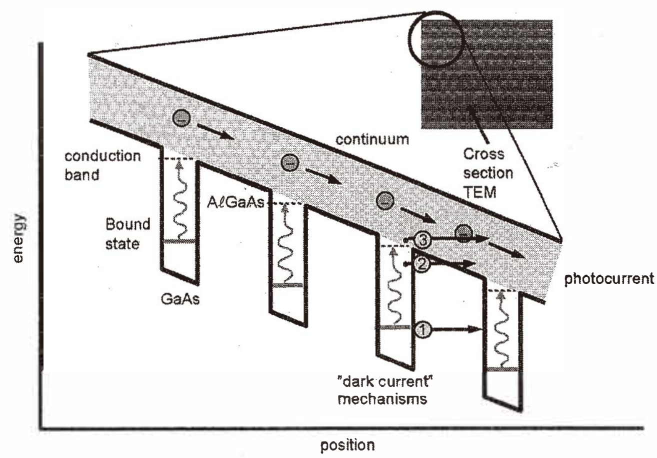

Fig. 1. Schematic diagram of the conduction band in a bound-to-quasibounᵀᴹd QWIP in an externally applied electric field. Absorption of IR photons can photoexcite electrons from the ground state of the quantum well into the continuum, causing a photocurrent. Three dark current mechanisms are also shown: ground state tunneling (1), thermally assisted tunneling (2), and thermionic emission (3). The inset shows a cross-sectional transmission electron micrograph of a QWIP sample.

tors because the wavelength of the peak response and cutoff can be continuously tailored by varying the layer thickness (quantum well width) and barrier composition (barrier height).

The lattice matched GaAs/$Al_xGa_{1-x}As$ material system is a very good candidate for creating such a quantum well structure, because the band gap of $Al_xGa_{1-x}As$ can be changed continuously by varying x (and hence the height of the quantum well). Thus, by changing the quantum well width L_w and the barrier height (Al molar ratio of $Al_xGa_{1-x}As$ alloy), this intersubband transition energy can be varied over a wide range, from short-wavelength infrared (SWIR; 1–3 μm), the mid-infrared (MWIR; 3–5 μm), through long-wavelength (LWIR; 8–12 μm) and into the VLWIR (>12 μm). It is important to note that, unlike intrinsic detectors which utilize interband transition, quantum wells of these detectors must be doped since the photon energy is not sufficient to create photocarriers ($h\nu < E_g$).

There are many ground based and space borne applications that require long-wavelength, large, uniform, reproducible, low cost, low 1/f noise, low power dissipation, and radiation hard infrared focal plane arrays (FPAs). For example, the absorption lines of many gas molecules, such as ozone, water, carbon monoxide, carbon dioxide, and nitrous oxide, occur in the wavelength region from 3 to 18 μm. Thus, infrared imaging systems that operate in the LWIR and VLWIR region are required in many space applications, such as monitoring global weather profiles, earth resource mapping, deforestation, and the distribution of minor constituents in the atmosphere, which are being planned for NASA's Earth Observing System.(2) In addition, 8–15 μm FPAs would be very useful in detecting cold objects such as ballistic missiles in midcourse [when the hot rocket engine is not burning most of the emission peaks in the 8–16 μm infrared region(3)]. The GaAs/$Al_xGa_{1-x}As$ material system allows the quantum well shape to be tweaked over a range wide enough to enable light detection at wavelengths longer than ~ 6 μm. Thus, GaAs-based QWIP is a potential candidate for such space borne and ground based applications, and many research groups(4–15) have already demonstrated large uniform FPAs of QWIPs tuned to detect light at wavelengths from 6 to 18 μm in the GaAs/$Al_xGa_{1-x}As$ material system.

2. Detectivity D^* Comparison

The blackbody detectivity D^*_B is basically the signal-to-noise ratio of a radiation detector normalized to unit area, and the operating bandwidth Δf of the detector is given by

$$D_B^* = R_B \frac{\sqrt{A \Delta f}}{i_n}, \tag{3}$$

with

$$R_B = \frac{\int_{\lambda 1}^{\lambda_2} R(\lambda)W(\lambda)d\lambda}{\int_{\lambda_1}^{\lambda_2} W(\lambda)d\lambda}, \tag{4}$$

where the responsivity R can be written in terms of absorption quantum efficiency η_a and photoconductive gain g as

$$R = (e/h\nu)\eta_a g. \tag{5}$$

The photoconductive gain of QWIPs can be written as

$$g = L/l, \tag{6}$$

where L is the hot electron mean free path and l is the length of the GaAs/AlGaAs MQW region.

The temporal noise current i_n of a single element radiation detector is given by

$$i_n = \sqrt{\beta e(I_D + I_P)g\Delta f}, \tag{7}$$

where e is the charge of an electron, β=2 for a photovoltaic detector (generation only) and β=4 for a photoconductor (generation and recombination), the photoconductive gain g =1 for a photovoltaic detector and g (QWIP) is typically 0.2 to 0.5 (depending on the device structure). I_D is the detector dark current and I_P is the detector photocurrent, given by

$$I_P = e\eta_a g\phi A, \tag{8}$$

where ϕ is the photon flux, (see refs. (18) and (25) for details) and (dP_B / dT) is the change in the incident integrated blackbody power in the spectral range of the detector with temperature. The integrated blackbody power P_B in the spectral range from λ_1 to λ_2 can be written as

$$P_B = A\sin^2\left(\frac{\theta}{2}\right)\cos\phi \int_{\lambda_1}^{\lambda_2} W(\lambda)d\lambda, \tag{9}$$

where θ, ϕ and W(λ) are the optical field of view, angle of incidence, and blackbody spectral density, respectively, and are defined by Eqs. (10) and (11),

$$P(\lambda) = W(\lambda)\sin^2(\theta/2)AF\cos\phi, \tag{10}$$

where A is the detector area, ϕ is the angle of incidence, θ is the optical field of view angle (i.e., $\sin^2(\theta/2) = (4f^2+1)^{-1}$ where f is the f number of the optical system; in this case θ is defined by the radius ρ of the blackbody opening at a distance D from the detector, so that $\tan(\theta/2) = \rho/D$), F represents all coupling factors and $F = T_f\,(1-r)C$ where T_f is the transmission of filters and windows, r = 28% is the reflectivity of the GaAs detector surface, C is the optical beam chopper factor (C = 0.5 in an ideal optical beam chopper), and W(λ) is the blackbody spectral density given by the following equation (i.e., the power radiated per unit wavelength interval at wavelength λ by a unit area of a blackbody at temperature T_B).

$$W(\lambda) = \left(2\pi c^2 h/\lambda^5\right)\left(e^{hc/\lambda kT_B} - 1\right)^{-1} \tag{11}$$

Consider a background limited condition. At this condition

$$I_D < I_P. \tag{12}$$

By combining equations (3), (5), (6), (7), (8) and (11) the detectivity D^* can be written as

$$D^* = \frac{1}{h\nu}\sqrt{\frac{\eta_a}{\beta\phi}}. \tag{13}$$

Thus,

$$\frac{D^*_{\mathrm{IDEAL}}}{D^*_{\mathrm{QWIP}}} = \sqrt{\frac{2\eta_{a,\mathrm{IDEAL}}}{\eta_{a,\mathrm{QWIP}}}}. \tag{14}$$

The lowest absorption quantum efficiency (η_a) of QWIP is typically 15% (including 30% reflection loss). The η_a of an ideal detector is 70% (assume 30% reflection loss). Thus eq. (13) reduces to

$$\frac{D^*_{\mathrm{IDEAL}}}{D^*_{\mathrm{QWIP}}} = 2.67. \tag{15}$$

Thus, this analysis clearly shows the photoconductive gain is irrelevant at a background limited operating condition and, therefore, the detectivities scales solely as a function of the absorption quantum efficiencies of the detectors.

3. Effect of Nonuniformity

The general figure of merit that describes the performance of a large imaging array is the noise equivalent temperature difference (NEΔT). NEΔT is the minimum temperature difference across the target that would produce a signal-to-noise ratio of unity and it is given by[16,17]

$$\mathrm{NE}\Delta T = \frac{\sqrt{A\Delta f}}{D^*_{\mathrm{B}}\,(dP_{\mathrm{B}}/dT)}. \tag{16}$$

Before discussing the array results, it is also important to understand the limitations on the FPA imaging performance due to pixel nonuniformities.[18] The total noise I_n of a focal plane array is given by

$$I_{\mathrm{n}} = i_{\mathrm{n}}^2 + u^2 (I_{\mathrm{P}} + I_{\mathrm{D}})^2, \tag{17}$$

where u is the nonuniformity of the focal plane array given by

$$u = \frac{\sigma}{\mu} = \frac{\sigma}{I_{\mathrm{P}} + I_{\mathrm{D}}}, \tag{18}$$

where μ is the mean total signal and σ is the standard deviation of the histogram of total signal vs number of pixels. Now the focal plane array detectivity or NEΔT can be obtained by the following equations:

$$D^*_{\mathrm{FPA}} = \frac{R\sqrt{A\Delta f}}{I_{\mathrm{n}}}, \tag{19}$$

$$\mathrm{NE}\Delta T_{\mathrm{FPA}} = \frac{\sqrt{A\Delta f}}{D^*_{\mathrm{FPA}}(dP_{\mathrm{B}}/dT)}, \tag{20}$$

where I_n is the total noise of the focal plane array given by eq. (17). The figures of merit such as D^*, NEΔT, NEP and NEI, are different representations of the basic signal-to-noise ratio of radiation detectors normalized in different ways. The signal-to-noise ratio of a focal plane array can be written as

$$SNR = \frac{I_{\mathrm{P}}}{I_{\mathrm{D}}} = \frac{I_{\mathrm{P}}}{\sqrt{i_{\mathrm{n}}^2 + u^2 (I_{\mathrm{P}} + I_{\mathrm{D}})^2}}. \tag{21}$$

Under the background limited condition (use eq. (12)) this reduces to

$$SNR \cong \frac{1}{u}. \tag{22}$$

This analysis clearly shows the importance of the array uniformity in the focal plane array total signal-to-noise ratio. This point has been discussed in detail by Shepherd[19] for the case of PtSi infrared FPAs[20] which have low response, but very high uniformity. The general figure of merit to describe the performance of a large imaging array is NEΔT, including the spatial noise which has been derived by Shepherd,[20] and this is given by

$$\mathrm{NE}\Delta T = \frac{N_\mathrm{n}}{dN_\mathrm{b} / dT_\mathrm{b}}, \tag{23}$$

where T_b is the background temperature, and N_n is the total number of noise electrons per pixel, given by

$$N_\mathrm{n}^2 = N_\mathrm{t}^2 + N_\mathrm{b} + u^2 N_\mathrm{b}. \tag{24}$$

The photoresponse independent temporal noise electrons are N_t, the shot noise electrons from the background radiation are N_b, and residual nonuniformity after correction by electronics is u. The temperature derivative of the background flux can be written to a good approximation as

$$\frac{dN_\mathrm{b}}{dT_\mathrm{b}} = \frac{hcN_\mathrm{b}}{\mathrm{k}\bar{\lambda}T_\mathrm{b}^2}, \tag{25}$$

where $\bar{\lambda}= (\lambda_1+\lambda_2)/2$ is the average wavelength of the spectral band between λ_1 and λ_2. When temporal noise dominates, NEΔT reduces to Eq. (16). In the case where residual nonuniformity dominates, Eqs. (23) and (25) reduce to

$$\mathrm{NE}\Delta T = \frac{u\bar{\lambda}T_\mathrm{b}^2}{1.44}. \tag{26}$$

The units of the constant are cm and °K; λ is in cm and T_b is in °K. Thus, in this spatial noise limited operation, NE$\Delta T \propto u$ and higher uniformity means higher imaging performance. Levine[18] has shown an example, taking T_b = 300°K, λ = 10 μm, and u = 0.1% leads to NEΔT = 63 mK, while an order of magnitude uniformity improvement (i.e., u = 0.01%) gives NEΔT = 6.3 mK. By using the full expression in Eq. (11), Levine[18] has calculated NEΔT as a function of D^* as shown in Fig. 2. It is important to note that when $D^* \geq 10^{10}$ cm$\sqrt{\mathrm{Hz}}$/W, the performance is uniformity limited and thus essentially independent of the detectivity, i.e., D^* is not the relevant figure of merit.[21]

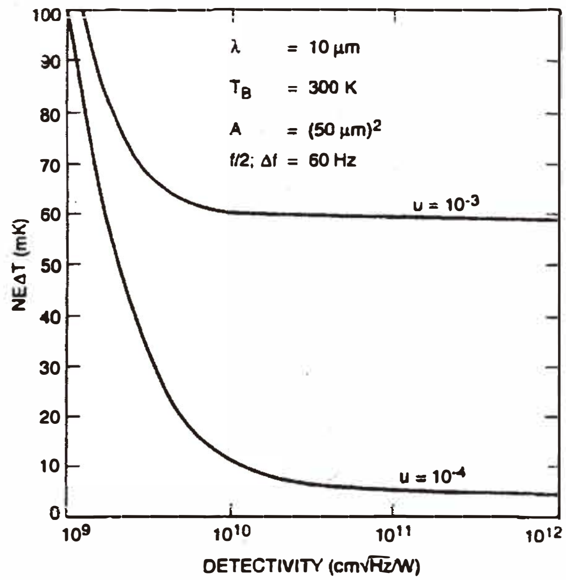

Fig. 2. Noise equivalent temperature difference NEΔT as a function of detectivity D*. The effects of nonuniformity are included for $u = 10^{-3}$ and 10^{-4}. Note that for $D^{*}>10^{10}$ cm÷Hz/W detectivity is not the relevant figure of merit for FPAs (taken from ref. (18)).

4. Commercially Available 320×256 LWIR Focal Plane Arrays

Infrared imaging systems that work in the 8–12 μm (LWIR) band have many applications, including night vision, navigation, flight control, and early warning systems. Several research groups have demonstrated[4–7,22–24] the excellent performance of QWIP arrays. For example, Faska *et al.*[8] have obtained very good images using a 256×256 bound-to-miniband MQW FPA. The first 256×256 LWIR hand-held imaging camera was demonstrated by Gunapala *et al.*[11] The device structure of this commercially available FPA consisted of a bound-to-quasibound QWIP containing 50 periods of a 45 Å well of GaAs (doped $n = 4\times10^{17}$ cm^{-3}) and a 500 Å barrier of $Al_{0.3}Ga_{0.7}As$. Ground state electrons are provided in the detector by doping the GaAs well layers with Si. This photosensitive MQW structure is sandwiched between 0.5 μm GaAs top and bottom contact layers doped to a level of $n = 5\times10^{17}$ cm^{-3} and grown on a semi-insulating GaAs substrate by MBE. Then a 0.7-μm-thick GaAs cap layer on top of a 300 Å $Al_{0.3}Ga_{0.7}As$ stop-etch layer was grown *in situ* on top of the device structure to fabricate the light-coupling optical cavity.

The detectors were back illuminated through a 45° polished facet as described earlier, and a responsivity spectrum is shown in Fig. 3. The responsivity of the detector peaks at 8.5 μm and the peak responsivity (R_p) of the detector is 300 mA/W at bias $V_B = -3$ V. The spectral width and the cutoff wavelength are $\Delta\lambda/\lambda = 10\%$ and $\lambda_c = 8.9$ μm, respectively. The measured absolute peak responsivity of the detector is small, up to about $V_B = -0.5$ V.

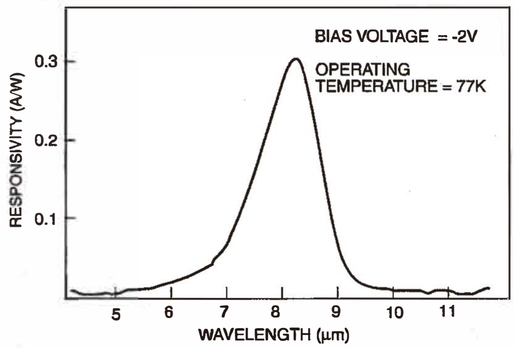

Fig. 3. Responsivity spectrum of a bound-to-quasibound LWIR QWIP test structure at temperature $T = 77$ K. The spectral response peak is at 8.3 μm and the long wavelength cutoff is at 8.8 μm.

Beyond that it increases nearly linearly with the bias reaching $R_p = 380$ mA/W at $V_B = -5$ V. This type of behavior of responsivity vs bias is typical for a bound-to-quasibound QWIP. The peak quantum efficiency was 6.9% at bias $V_B = -1$ V for a 45° double pass. The lower quantum efficiency is due to the lower well doping density (5×10^{17} cm^{-3}) as it is necessary to suppress the dark current at the highest possible operating temperature.

After the 2D grating reflector array was defined by lithography and dry etching, the photoconductive QWIPs of the 320×256 FPAs were fabricated by wet chemical etching through the photosensitive GaAs/$Al_xGa_{1-x}As$ MQW layers into the 0.5-μm-thick doped GaAs bottom contact layer. The pitch of the FPA is 30 μm and the actual pixel size is 28×28 μm^2. The 2D grating reflectors on top of the detectors were then covered with Au/Ge and Au for ohmic contact and reflection. A single QWIP FPA was chosen and hybridized (via an indium bump-bonding process) to a 320×256 CMOS readout multiplexer (Indigo-ISC9705) and biased at $V_B = -2.0$ V. The FPA was back-illuminated through the flat thinned substrate membrane (thickness≈1300 Å). This array gave excellent images with 99.98% of the pixels working (number of dead pixels≈10), demonstrating the high yield of GaAs technology.[11] The measured NEΔT (mean value) of the FPA at an operating temperature of $T = 70$°K, bias $V_B = -2$ V, and 300°K background is 33 mK. This agrees reasonably with our estimated value of 30 mK based on test structure data.

A 320×256 QWIP FPA hybrid was mounted onto a 84-pin leadless chip carrier and installed into a laboratory dewar which was cooled by liquid nitrogen, to demonstrate a LWIR imaging camera. The FPA was tested at temperatures 65, 70, and 75°K. Lower cryogenic temperatures were achieved by pumping on liquid nitrogen and the temperature was stabilized by regulating the pressure of gaseous nitrogen. The other element of the camera is a 100 mm focal length germanium lens with a 5.5 degree field of view. It is designed to be transparent in the 8–12 μm wavelength range to be compatible with the QWIP's 8.5 μm operation. The digital acquisition resolution of the camera is 12-bits, which determines the instantaneous dynamic range of the camera (i.e., 4096). However, the dynamic range of QWIP is 85 decibels. The NEΔTs of these FPAs were measured as a function of operating temperature and the results are shown in Fig. 4.

5. 640×486 Long-Wavelength QWIP Camera

To detect LWIR radiation we have designed the following MQW structure. Each period of the MQW structure consists of a 45 Å well of GaAs (doped $n = 4\times10^{17}$ cm^{-3}) and a 500 Å barrier of $Al_{0.3}Ga_{0.7}As$. Stacking many identical quantum wells (typically 50) together increases photon absorption. This photosensitive MQW structure is sandwiched between 0.5 μm GaAs top and bottom contact layers doped at a density of $n = 5\times10^{17}$ cm^{-3} and grown on a semi-insulating GaAs substrate by molecular beam epitaxy (MBE). Then a 0.7-μm-thick-GaAs cap layer on top of a 300 Å $Al_{0.3}Ga_{0.7}As$ stop-etch layer was grown *in situ* on top of the device structure to fabricate the light-coupling optical cavity.

The responsivity of the detector peaks at 8.5 μm, and the peak responsivity (R_p) of the detector is 300 mA/W at bias $V_B = -3$ V. The spectral width and the cutoff wavelength are $\Delta\lambda/\lambda = 10\%$ and $\lambda_c = 8.9$ μm, respectively. The peak quantum efficiency is 6.9% at bias $V_B = -1$ V for a 45° double pass. The lower quantum efficiency is due to the lower well doping density (5×10^{17} cm^{-3}), as it is necessary to suppress the dark current at the highest possible operating temperature.[25]

After the 2D grating array was defined by photolithography and dry etching, the photoconductive QWIPs of the 640×486 focal plane arrays (FPAs) were fabricated by wet chemical etching through the photosensitive GaAs/$Al_xGa_{1-x}As$ MQW layers into the 0.5-μm-thick doped GaAs bottom contact layer. The pitch of the FPA is 25 μm and the actual pixel size is 18×18 μm^2. The cross gratings on top of the detectors were then covered with Au/Ge and Au for ohmic contact and reflection. A single QWIP FPA was chosen and hybridized to a 640×486 direct injection silicon readout multiplexer and biased at $V_B = -2.0$ V. The FPA was back-illuminated through the flat thinned substrate membrane (thickness ≈1300 Å). This thinned GaAs FPA membrane has completely eliminated the thermal mismatch between the silicon CMOS readout multiplexer and the GaAs-based QWIP FPA. Basically, the thinned GaAs-based QWIP FPA membrane adapts to the thermal

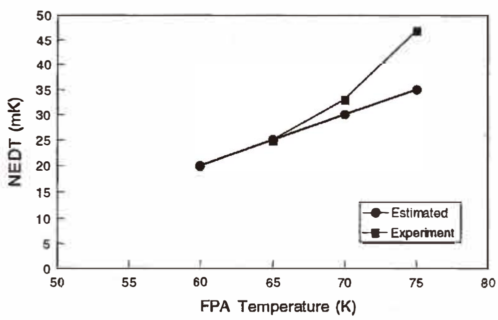

Fig. 4. NEDT of 320×256 QWIP focal plane array as a function of operating temperature.

expansion and contraction coefficients of the silicon readout multiplexer. Therefore, this thinning has played an extremely important role in the fabrication of the large area FPA hybrids. In addition, this thinning has completely eliminated the pixel-to-pixel optical cross-talk of the FPA. This initial array gave excellent images with 99.9% of the pixels working, demonstrating the high yield of GaAs technology.

A 640×486 QWIP FPA hybrid was mounted onto a 84-pin leadless chip carrier and installed into a laboratory dewar which was cooled by liquid nitrogen, to demonstrate a LWIR imaging camera.(12) The experimentally measured mean NEΔT of the QWIP camera is 36 mK at an operating temperature of T = 70°K and bias $V_B = -2$ V at a 300°K background. This agrees reasonably with our estimated value of 25 mK based on single element test structure data. The uncorrected NEΔT nonuniformity of the 640×486 FPA is about 5.6% (= sigma/ mean).

Video images were taken at a frame rate of 30 Hz at temperatures as high as T = 70°K using a ROC capacitor having a charge capacity of 9×10^6 electrons. The nonuniformity after two-point (17° and 27° Celsius) correction improves to an impressive 0.03%. Figure 5 shows a frame of video image taken with this long-wavelength 640×486 QWIP camera. This image demonstrates the high sensitivity of the 640×486 long-wavelength QWIP staring array camera.(12) As mentioned earlier, this high yield is due to the excellent GaAs growth uniformity and the mature GaAs processing technology.

6. 640×486 Long-Wavelength Dualband Imaging Camera

The LWIR and very long-wavelength infrared (VLWIR) dualband QWIP device structure described in this section is processed to interlace simultaneously readable dualband FPAs (i.e., odd rows for one color and even rows for the other color).(26)

The device structure consists of a 30 periods stack of VLWIR QWIP structures and a

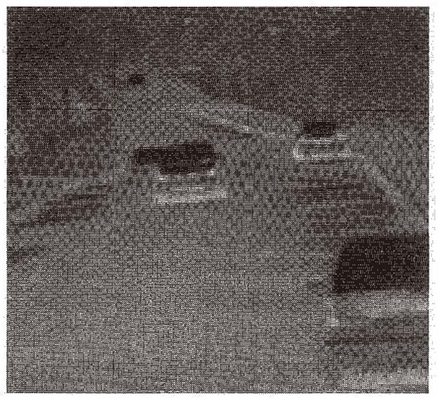

Fig. 5. This picture was taken at night (around midnight) and it clearly shows where automobiles were parked during the day time. This image demonstrates the high sensitivity of the 640×486 long-wavelength QWIP staring array camera (taken from ref. (12)).

second 18 periods stack of LWIR QWIP structures separated by a heavily doped 0.5-μm-thick intermediate GaAs contact layer. The first stack (VLWIR) consists of 30 periods of a 500 Å $Al_xGa_{1-x}As$ barrier and a 60 Å GaAs well. Since the dark current of this device structure is dominated by the longer wavelength portion of the device structure, the VLWIR QWIP structure has been designed to have a bound-to-quasibound intersubband absorption[25] peak at 14.5 μm. The second stack (LWIR) consists of 18 periods of a 500 Å $Al_xGa_{1-x}As$ barrier and a narrow 40 Å GaAs well. This LWIR QWIP structure has been designed to have a bound-to-continuum intersubband absorption peak at 8.5 μm, since the photocurrent and dark current of the LWIR device structure is relatively small compared to the VLWIR portion of the device structure. This whole dualband QWIP structure is then sandwiched between 0.5 μm GaAs top and bottom contact layers doped at a density of $n = 5{\times}1017$ cm^{-3}, and were grown on a semi-insulating GaAs substrate by MBE. Then a 300 Å $Al_{0.3}Ga_{0.7}As$ stop-etch layer and a 1.0-μm-thick GaAs cap layer were grown ***in situ*** on top of the device structure. GaAs wells of the LWIR and VLWIR stacks were doped at densities of $n = 6{\times}10^{17}$ and $2.5{\times}10^{17}$ cm^{-3}, respectively. All contact layers were doped to $n = 5{\times}10^{17}$ cm^{-3}. The GaAs well doping density of the LWIR stack was intentionally increased by a factor of two to compensate for the reduced number of quantum wells in the LWIR stack.[26] It is worth noting that the total (dark current + photo- current) current of each stack can be independently controlled by carefully designing the position of the upper state, the doping densities of the wells, and the number of periods in each MQW stack. All of these features were utilized to obtain approximately equal total currents from each MQW stack.

Simultaneously measured responsivity spectra of these vertically integrated dualband QWIPs are shown in Fig. 6. Based on single element test detector data, the LWIR detectors show BLIP at bias $V_B = -2$ V and temperature $T = 72$°K for a 300°K background with f/2 cold stop. The VLWIR detectors show BLIP under the same operating conditions

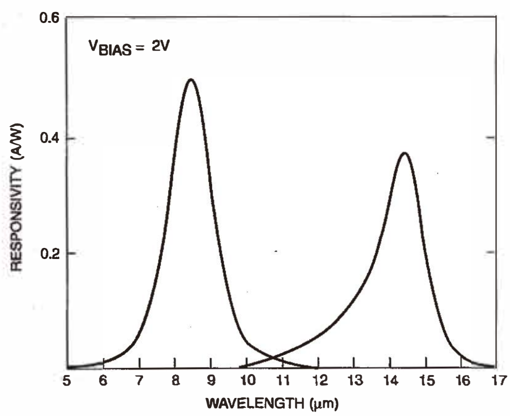

Fig 6. Simultaneously measured responsivity spectra of vertically integrated LWIR and VLWIR dualband QWIP detector (taken from ref. (26)).

at a 45°K operating temperature.[26] Two different 2D periodic grating structures were designed to independently couple the 8–9 and 14–15 μm radiation into detector pixels in even and odd rows of the FPAs. The FPA fabrication process is described elsewhere.[26]

These dualband FPAs were tested at a background temperature of 300°K with a f/2 cold stop and at a 30 Hz frame rate. As expected (due to BLIP), the estimated and experimentally obtained NEΔT values of the LWIR detectors do not change significantly at temperatures below 65°K. The estimated NEΔT values of LWIR and VLWIR detectors at 40°K are 36 and 44 mK, respectively (see Figs. 7 and 8). These estimated NEΔT values based on the test detector data agree reasonably well with the experimentally obtained values. The experimental LWIR NEΔT value is lower than the estimated NEΔT value of 36 mK. This improvement is attributed to the 2D periodic grating light-coupling efficiency. On the other hand, the experimental VLWIR NEΔT value is higher than the estimated NEΔT value of 44 mK. The authors believe this degradation is due to inefficient light coupling in the 14–15 μm region, readout multiplexer noise, and noise of the proximity electronics. At 40°K the performance of both LWIR and VLWIR detector pixels of this dualband FPA are limited by photocurrent noise and readout noise.

Video images were taken at a frame rate of 30 Hz, at temperatures as high as $T = 74$°K, using a ROC capacitor having a charge capacity of 9×10^6 electrons (the maximum number of photoelectrons and dark electrons that can be counted in the time taken to read each detector pixel). Figure 9 shows simultaneously acquired 8–9 and 14–15 micron images using this two-color camera.[26]

7. Broad-Band QWIPs

A broad-band MQW structure can be designed by repeating a unit of several quantum wells with slightly different parameters such as quantum well width and barrier height. The first device structure (shown in Fig. 10) demonstrated by Bandara *et al.*[27] has 33 repeated layers of GaAs three-quantum-well units separated by LB ~ 575-Å-thick $Al_xGa_{1-x}As$ barriers.[28] The thicknesses of the quantum wells of the three-quantum-well units are designed to respond at peak wavelengths around 13, 14 and 15 μm, respectively. These quantum wells are separated by 75-Å-thick $Al_xGa_{1-x}As$ barriers. The Al mole fraction (x) of barriers throughout the structure was chosen such that the $\lambda_p = 13$ μm quantum well operates under bound-to-quasibound conditions. The excited state energy level broadening was further enhanced due to overlap of the wave functions associated with the excited states of quantum wells separated by thin barriers. Energy band calculations based on a two-band model show excited state energy levels spreading about 28 meV. An experimentally measured responsivity curve at $V_B = -3$ V bias voltage has shown broadening of the spectral response up to $\Delta\lambda \sim 5.5$ μm, i.e., the full-width at half maximum from 10.5–16 μm. This broadening $\Delta\lambda/\lambda_p \sim 42\%$ is about a 400% increase compared to a typical bound-to-quasibound QWIP (see Fig. 11).

This detector has been developed specifically for thermal infrared imaging spectrometers—anticipating a possible need for Mars exploration. This program required a thermal infrared imaging spectrometer with minimum power, mass, and volume. One attractive concept involved a spatially modulated infrared spectrometer (SMIS) to cover

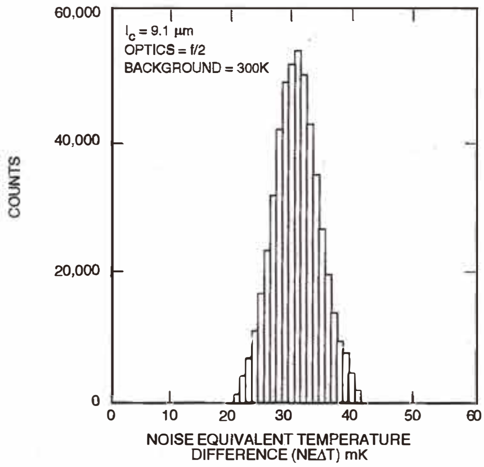

Fig 7. The uncorrected NEDT histogram of 8–9 μm detector pixels of the 640×486 dualband FPA. The mean NEDT is 29 mK.

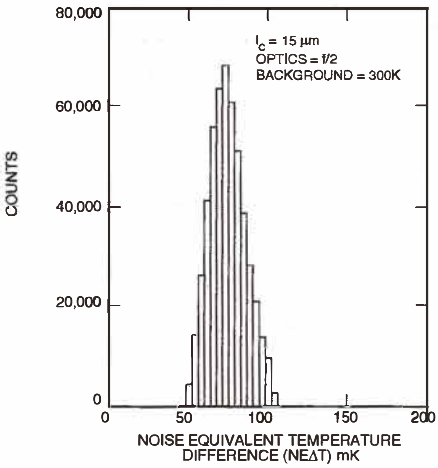

Fig 8. The uncorrected NEDT histogram of 14–15 μm detector pixels of the 640×486 dualband FPA. The mean NEDT is 74 mK.

the LWIR and VLWIR spectral ranges. This instrument does not contain any moving mirrors because it uses the spatially modulated Fourier transform spectroscopy technique. Another advantage of this concept is that it has a substantially higher signal flux because all of the photons entering the pupil are used. The high spectral resolution version of this instrument requires larger format FPAs (at least 640×486) with high pixel-to-pixel uniformity. The lack of large format, uniform LWIR and VLWIR FPA technology has

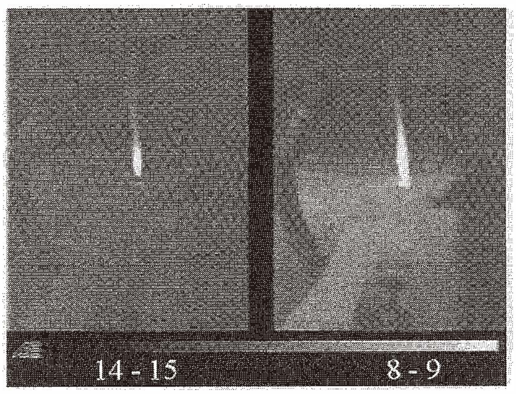

Fig. 9. Both pictures show (flame — simultaneously acquired) two-color images with the 640×486 two-color QWIP camera. Image on the left is from 14–15 micron infrared and the image on the right is from 8–9 micron infrared. Pixel pitch of the FPA is 25 micron. The 14–15 micron image is less sharp due to the diffraction limited spot size being larger than the pixel pitch of the FPA (taken from ref. (26)).

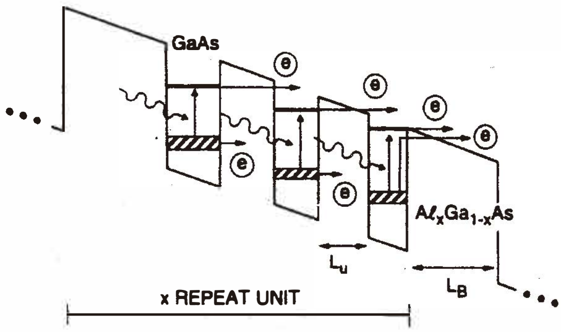

Fig. 10. Schematic diagram of the conduction band in broadband QWIP in an externally applied electric field. The device structure consists of 33 repeated layers of three-quantum-well units separated by thick $Al_xGa_{1-x}As$ barriers. Also shown are the possible paths of dark current electrons and photocurrent electrons of the device under a bias (taken from ref. (27)).

prevented the development of such highly sensitive and robust thermal infrared spectrometers. That has changed recently due to demonstration of highly uniform, large format QWIP FPAs with lower 1/f noise at a lower cost than any other LWIR detector. In addition, the use of external filters can be avoided because QWIP can be designed to have sharp spectral cut-offs at required wavelengths. Francis Reininger at JPL has demonstrated this concept by building a prototype laboratory instrument working with a 8–9 μm QWIP 640×486 FPA. The unique characteristic of this instrument (besides being small

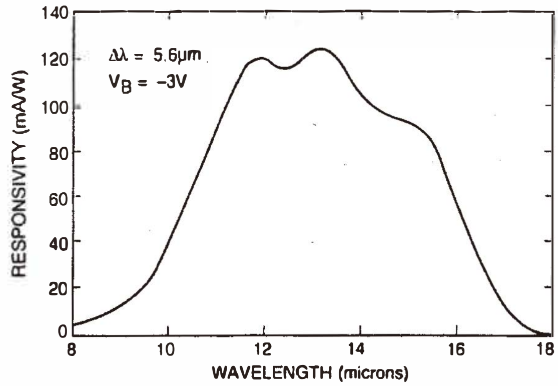

Fig. 11. Experimental measurements of the normalized responsivity spectrum of 10–16 μm broad-band QWIP at bias voltage V_B = –4 V (taken from ref. (28)).

and efficient) is that it has one instrument line shape for all spectral colors and spatial field positions. Using broad-band QWIP arrays with wavelengths out to 16 μm, the next version of this instrument could become the first compact, high-resolution thermal infrared, hyper-spectral imager with a single spectral line shape and zero spectral smile. Such an instrument is in strong demand by scientists studying the Earth and planetary science.

8. Applications

8.1 *Fire Fighting*

Video images were taken at a frame rate of 60 Hz at temperatures as high as T = 70°K using a ROC capacitor having a charge capacity of 9×10^6 electrons (the maximum number of photoelectrons and dark electrons that can be counted in the time taken to read each detector pixel). This infrared camera helped a Los Angeles TV news crew get a unique perspective on fires that raced through the Southern California seaside community of Malibu in October, 1996. The camera was used on the TV station's news helicopter. This portable camera features infrared detectors which cover longer wavelengths than previous portable cameras. This allows the camera to see through smoke and pinpoint lingering hotspots which are not normally visible. This enabled the TV station to transmit live images of hotspots in areas which appeared innocuous to the naked eye. These hotspots were a source of concern and difficulty for firefighters, because they could flare up even after the fire appeared to have subsided. Figure 12 shows the comparison of visible and infrared images of an area just burned as seen by the news crew at nighttime. It works effectively in both daylight and nighttime conditions. The event marked the QWIP camera's debut as a fire observing device.

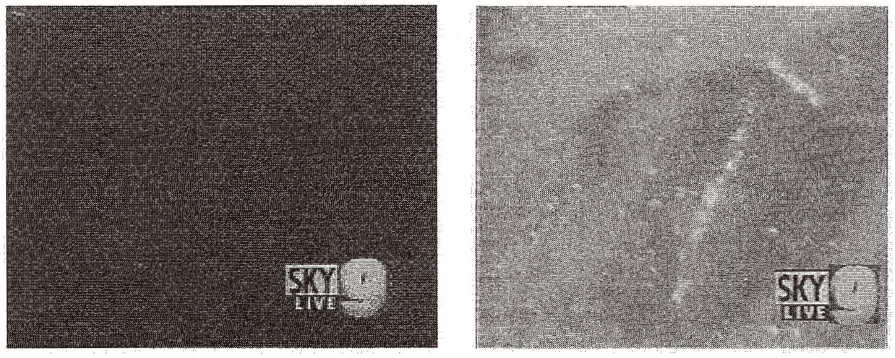

(a) (b)

Fig. 12. Comparison of visible and infrared images of a recently burned area as seen by a highly sensitive visible CCD camera and the long-wavelength infrared camera in nighttime. (a) Visible image from a CCD camera and (b) image from the 256×256 portable QWIP camera. This portable camera featuring infrared detectors covers longer wavelengths than previous portable cameras. This allows the camera to see through smoke and pinpoint lingering hotspots which are not normally visible. This enables firefighters to locate hotspots in areas which appear innocuous to the naked eye. These hotspots are a source of concern and difficulty for firefighters, because fire can flare up even after it appears to have subsided. The camera works effectively in both daylight and nighttime conditions.

8.2 *Volocanology*

Recently, the camera has been used to observe volcanoes, mineral formations, weather and atmospheric conditions. The QWIP camera was taken to Mt. Kilauea, a volcano in Hawaii. The objectives of this trip were to map geothermal features. The wide dynamic range enabled us to image volcanic features at temperatures much higher (300–1000°C) than can be imaged with conventional thermal imaging systems in the 3–5 μm range or in visible. Figure 13 shows a comparison of visible and infrared images of Mt. Kilauea in Hawaii. The infrared image of the volcano clearly shows a hot lava tube running underground which is not visible to the naked eye.

8.3 *Medicine*

Studies have determined that cancer cells exude nitric oxide. This causes changes in blood flow in the tissue surrounding cancer that can be detected by a sensitive thermal sensor. Recently, OmniCorder Technologies, Inc., Stony Brook, N.Y. has developed an instrument called the BioScan System™ based on JPL developed QWIP FPA technology. In this instrument a mid-format QWIP FPA is used for dynamic area telethermometry (DAT).[29] DAT has been used to study the physiology and patho-physiology of cutaneou perfusion, which has many clinical applications. DAT involves the accumulation of hundreds of consecutive infrared images and fast Fourier transform (FFT) analysis of the biomodulation of skin temperature and of the microhomogeneity of skin temperature

(a) (b)

Fig. 13. Comparison of visible and infrared images of the Mount Kilauea Volcano in Hawaii. (a) Visible image from a highly sensitive CCD camera. (b) Image from the 256×256 portable QWIP camera. The wide dynamic range enabled us to image volcanic features at temperatures much higher (300 –1000°K) than can be imaged with conventional thermal imaging systems in the 3–5 μm range or in the visible. The infrared image of the volcano clearly show a hot lava tube running underground which is not visible to the naked eye. This demonstrates the advantages of long wavelength infrared in geothermal mapping.

(HST, which measures the perfusion of the skin's capillaries). The FFT analysis yields the thermoregulatory frequencies and amplitudes of temperature and HST modulation.

To obtain reliable DAT data, one needs an infrared camera in the >8 μm range (to avoid artifacts of reflections of modulated emitters in the environment), a repetition rate of 30 Hz (allowing accumulation of a maximal number of images during the observation period to maximize the resolution of the FFT), frame to frame instrumental stability (to avoid artifacts stemming from instrument modulation), and sensitivity of less than 30 mK. According to these researchers the longer wavelength operation, higher spatial resolution, higher sensitivity and greater stability of the QWIP FPAs made it the best choice among all infrared FPAs. The two technologies work together to image the target area and to provide the physician with immediate diagnostic information. It causes no discomfort to the patient and uses no ionizing radiation. Basically, the digital sensor detects the infrared energy emitted from the body, thus "seeing" the minute differences associated with blood flow changes.

In December 1999, the Food and Drug Administration issued clearance to market the BioScan System™ for breast tumor detection and other medical applications. This cancer detection instrument is currently being tested by the Dana-Farber Cancer Institute, Boston, MA, for its use in monitoring the effectiveness of cancer treatment in patients. The BioScan System™ has been used to locate and confirm the presence of a cancerous breast lesion by detecting the cancer's ability to recruit a new blood supply, one of the hallmarks of a malignant lesion. The goal of the Dana-Farber research is to evaluate the

BioScan System's ability to monitor biological effects of cancer treatment and to help physicians detect treatment-induced changes in cancerous lesions of the breast, skin and other organs. Armed with this information, they can better determine the effectiveness of the treatments.

This camera has also been used by a group of researchers at the University of Southern California in brain surgery, skin cancer detection, and leprosy patients. In brain tumor removal a sensitive thermal imager can help surgeons to find small capillaries that grow towards the tumor due to angeogenisis (see Fig. 14). In general cancerous cells have a high metabolic rate and these cancerous cells recruit a new blood supply, one of the characteristics of a malignant lesion. Therefore, cancerous tissues are slightly warmer than the neighboring healthy tissues. Thus, a sensitive thermal imager can easily detect malignant skin cancers (see Figs. 15(a) and 15(b))(p.21). Figure 16 clearly shows the temperature gradient in the foot of a leprosy patient.

8.4 *Defense*

It is not necessary to explain how real-time infrared imaging is important in surveillance, reconnaissance and military operations. The QWIP RADIANCE was used by the researchers at the Ballistic Missile Defense Organization's innovative science and technology experimental facility in a unique experiment to discriminate and clearly distinguish a cold launch vehicle from the hot plume emanating from rocket engines.

Usually, the temperature of cold launch vehicles is about 250°K, whereas the temperatures of the hot plume emanating from a launch vehicle can reach 950°K. According to Plank's blackbody emission theory, the photon flux ratio of 250°K and 950°K blackbodies at 4 μm is about 25,000, whereas the same photon flux difference at 8.5 μm is about 115 (see Fig. 17). Therefore, it is very clear that one must explore longer wavelengths for better cold-body vs hot plume discrimination, because the highest instantaneous dynamic range of infrared cameras is usually 12-bits (i.e., 4096) or less. Figure 18 shows an image of a Delta-II launch taken with a QWIP RADIANCE camera. This clearly indicates the advantage of long-wavelength QWIP cameras in the discrimination and identification of cold launch vehicles in the presence of hot plumes during early stages of launch.

8.5 *Astronomy*

In this section we discuss the first astronomical observations with a QWIP FPA. To perform this astronomical observation we have designed a QWIP wide-field imaging multicolor prime focus infrared camera (QWICPIC). Observations were conducted at the five meter Hale telescope at Mt. Palomar with QWICPIC based on 8–9 μm 256×256 QWIP FPA operating at T=35°K. The ability of QWIPs to operate under high photon backgrounds without excess noise enables the instrument to observe from the prime focus with a wide 2"×2" field of view, making this camera unique among the suite of infrared instruments available for astronomy. The excellent 1/f noise performance (see Fig. 19) of QWIP FPAs allows QWICPIC to observe in a slow scan strategy often required in infrared observations from space.

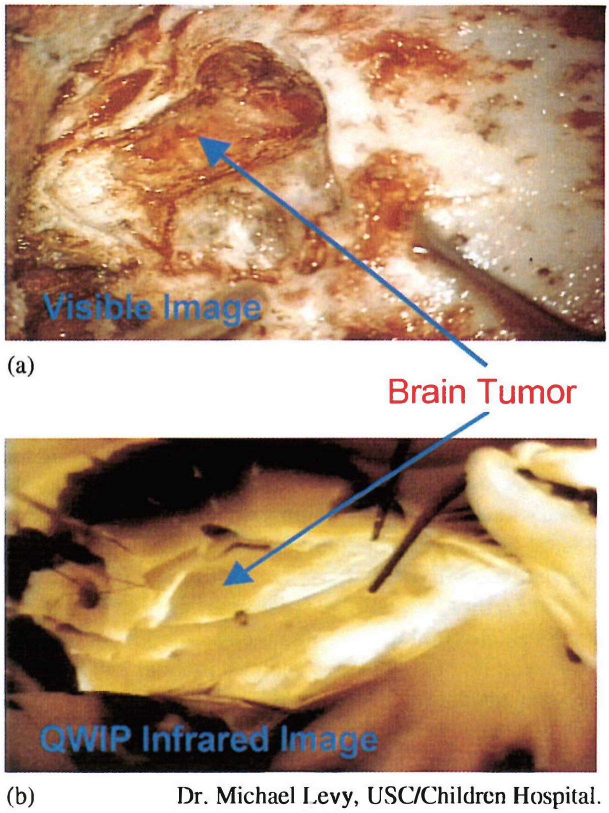

Fig. 14. (a) Visible image of a brain tumor (most of the cancerous cells are dead due to cancer treating drugs). (b) The thermal infrared image clearly discriminates the healthy tissues from dead tissues.

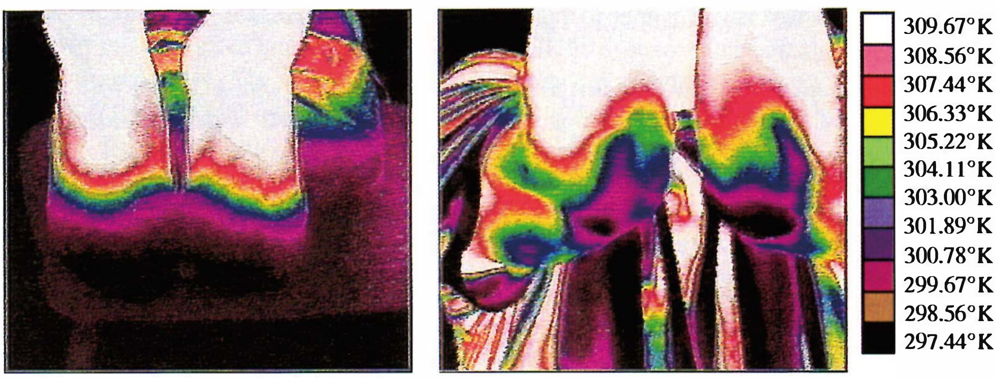

Fig. 16. This figure shows the temperature variation in the toes and elbows of a leprosy patient.

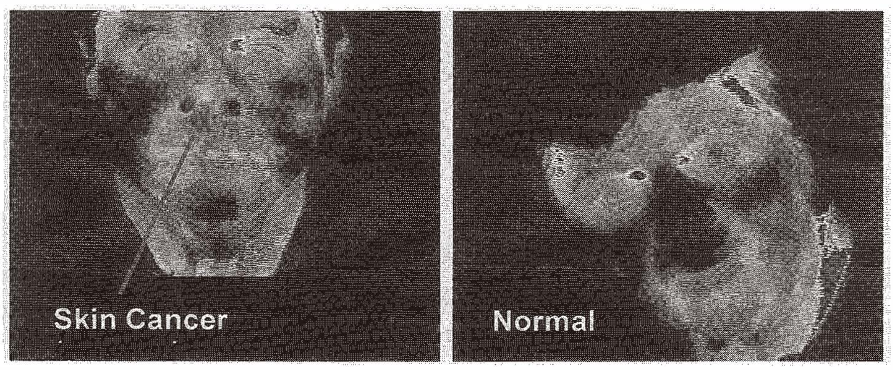

(a) (b)

Fig. 15. (a) This clearly shows the tip of the nose is warmer than its surrounding tissues due to the enhanced metabolic activity (angiogenesis) of skin cancer. (b) shows a face with no skin cancer on the nose. Usually, the nose and ears are colder than the other parts of the face, because they extend away from the body.

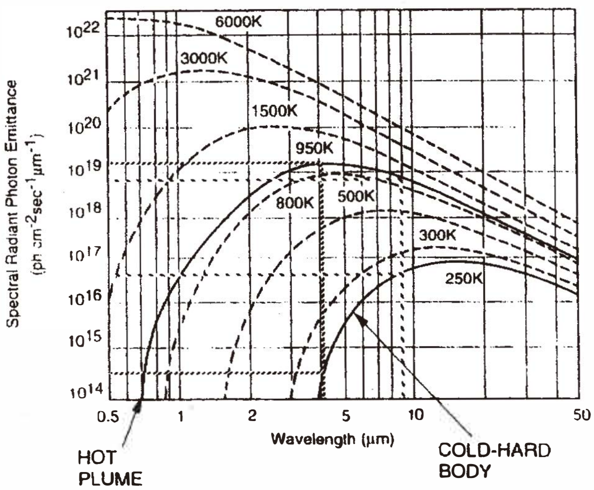

Fig. 17. Blackbody spectral radiant photon emittance at various temperatures.

Figure 20 compares an image of a composite near-infrared image (a) obtained by 2MASS, with an 8.5 μm long-wavelength infrared image (b) obtained with a QWIP focal plane array at the primary focus of the Palomar 200-inch Hale telescope. The S106 region displays vigorous star-formation obscured behind dense molecular gas and cold dust, and extended nebular emission from dust heated by starlight. Thermal-infrared imaging can be used to assess the prevalence of warm (~300°K) dusty disks surrounding stars in such regions. Formation of these disks is an evolutionary step in the development of planetary

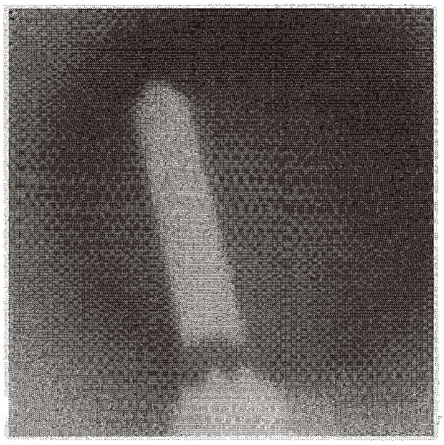

Fig. 18. Image of a Delta-II launch vehicle taken with the long-wavelength QWIP RADIANCE during the launch. This clearly indicates the advantage of long-wavelength QWIP cameras in the discrimination and identification of cold launch vehicles in the presence of hot plumes during the early stages of a launch.

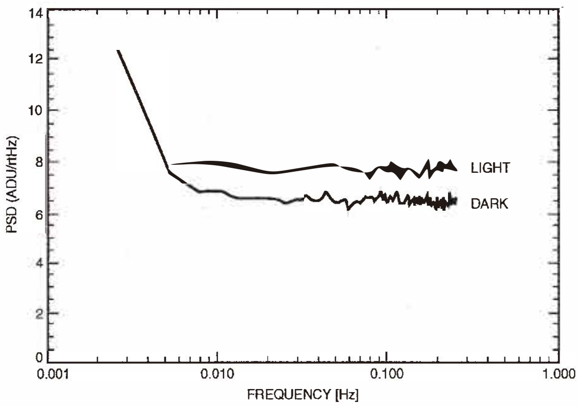

Fig. 19. 1/f noise spectrum of 8–9 μm 256×256 QWIP focal plane array. (1 ADU = 430 electrons). This clearly shows that QWIPs have no 1/f down to 30 mHz. This allows QWIP-based instruments to use longer integration times and frame adding capability.

systems. These images demonstrate the advantage of large format, stable (low 1/f noise) LWIR QWIP FPAs for surveying obscured regions in search of embedded or reddened objects such as young forming stars.

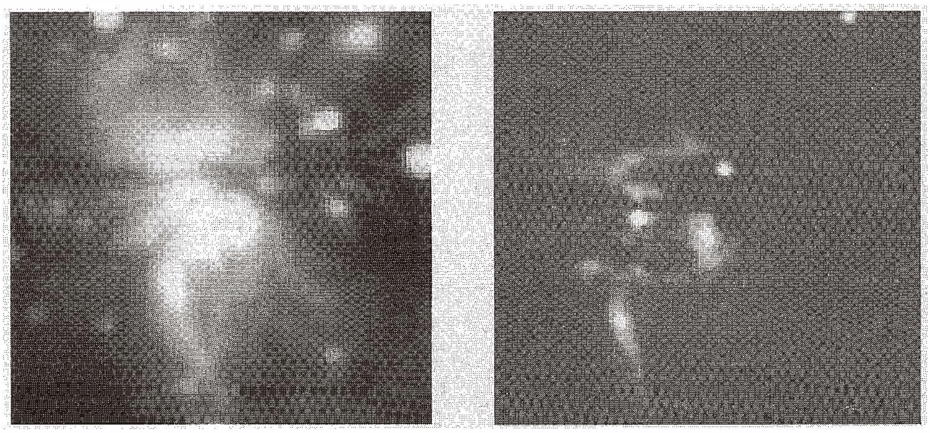

(a) (b)

Fig. 20. Comparison of (a) a composite near-infrared image obtained by 2MASS, with (b) an 8.5 μm long-wavelength infrared image obtained with a QWIP focal plane array at the primary focus of the Palomar 200-inch Hale telescope. The S106 region displays vigorous star-formation obscured behind dense molecular gas and cold dust, and extended nebular emissions from dust heated by starlight. Thermal-infrared imaging can be used to assess the prevalence of warm (~300°K) dusty disks surrounding stars in such regions. Formation of these disks is an evolutionary step in the development of planetary systems.

9. Summary

In summary, we have discussed the importance of FPA uniformity in NEΔT, the general figure of merit that describes the performance of large imaging arrays. It is important to note that when $D^* \geq 10^{10}$ cm $\sqrt{\text{Hz}}$/W, the performance is uniformity limited and thus essentially independent of the detectivity, i.e., D^* is not the relevant figure of merit.(18,21) Furthermore, we have demonstrated the usefulness of the long-wavelength 320×256 commercial QWIP FPAs based on the bound-to-quasibound device structure, the 648×486 long-wavelength camera, the 640×486 dualband imaging camera, and several applications in science, medicine and defense.

Acknowledgments

The research described in this paper was performed by the Center for Space Microelectronics Technology, Jet Propulsion Laboratory, California Institute of Technology, and was jointly sponsored by the JPL Director's Research and Development Fund, the Ballistic Missile Defense Organization/Innovative Science & Technology Office, the Breakthrough Sensors and Instrument Component Technology Thrust of the NASA Cross Enterprise Technology Development Program and the Air Force Research Laboratory.

References

1 C. Weisbuch: Semicon. Semimet. **24** (1987) 1–133.
2 M. T. Chahine: Proceedings of Innovative Long Wavelength Infrared Detector Workshop (Pasadena, California, USA, 1990) 3–31.
3 D. Duston: BMD Monitor (1995) 180–183.
4 C. G. Bethea, B. F. Levine, V. O. Shen, R. R. Abbott and S. J. Hseih: IEEE Trans. Electron Devices **38** (1991) 1118.
5 C. G. Bethea and B. F. Levine: Proceedings of SPIE International Symposium on Optical Applied Science and Engineering (San Diego, CA, USA, 1992).
6 C. G. Bethea, B. F. Levine, M. T. Asom, R. E. Leibenguth, J. W. Stayt, K. G. Glogovsky, R. A. Morgan, J. Blackwell and W. Parish: IEEE Trans. Electron Devices **40** (1993) 1957.
7 L. J. Kozlowski, G. M. Williams, G. J. Sullivan, C. W. Farley, R. J. Andersson, J. Chen, D. T. Cheung, W. E. Tennant and R. E. DeWames: IEEE Trans. Electron. Devices ED–**38** (1991) 1124.
8 T. S. Faska, J. W. Little, W. A. Beck, K. J. Ritter, A. C. Goldberg and R. LeBlanc: Innovative Long Wavelength Infrared Detector Workshop (Pasadena, CA, USA, 1992).
9 W. A. Beck, T. S. Faska, J. W. Little, J. Albritton and M. Sensiper: Proceedings of the Second International Symposium on 2–20 μm Wavelength Infrared Detectors and Arrays, Physics and Applications (Miami Beach, Florida, USA, 1994).
10 S. D. Gunapala, J. S. Park, G. Sarusi, T.-L. Lin, J. K. Liu, P. D. Maker, R. E. Muller, C. A. Shott and T. Hoelter: IEEE Trans. Electron Devices, **44** (1997) 45–50 .
11 S. D. Gunapala, J. K. Liu, J. S. Park, M. Sundaram, C. A. Shott, T. Hoelter, T.-L. Lin, S. T. Massie, P. D. Maker, R. E. Muller and G. Sarusi: IEEE Trans. Electron Devices **44** (1997) 51–57 .
12 S. D. Gunapala, S. V. Bandara, J. K. Liu, W. Hong, M. Sundaram, P. D. Maker, R. E. Muller, C. A. Shott and R. Carralejo: IEEE Trans. Electron Devices **45** (1998) 1890.
13 J. Y. Andersson, J. Alverbro, J. Borglind, P. Helander, H. Martijn and M. Ostlund: SPIE **3061** (1997) 740–748 .
14 K. K. Choi, A. C. Goldberg, N. C. Das, M. D. Jhabvala, R. B. Bailey and K. Vural: SPIE **3287** (1998) 118–127.
15 R. Breiter, W. Cabanski, R. Koch, W. Rode, and J. Ziegler: SPIE **3379** (1998) 423 .
16 R. H. Kingston: Detection of Optical and Infrared Radiation (Springer, Berlin, 1978).
17 A. Zussman, B. F. Levine, J. M. Kuo and J. de Jong: J. Appl. Phys. **70** (1991) 5101 .
18 B. F. Levine: J. Appl. Phys. **74** R1 (1993).
19 F. D. Shepherd: SPIE **930** (Orlando, FL, USA, 1988) 2.
20 J. M. Mooney, F. D. Shepherd, W. S. Ewing, J. E. Murgia and J. Silverman: Opt. Eng. **28** (1989) 1151 .
21 I. Grave and A. Yariv: Intersubband Transitions in Quantum Wells, eds. E. Rosencher, B. Vinter and B. Levine, Cargese, France (Plenum, New York, 1992) p. 15.
22 B. F. Levine, C. G. Bethea, K. G. Glogovsky, J. W. Stayt and R. E. Leibenguth: Semicond. Sci. Technol. **6** C114 (1991).
23 M. T. Asom, C. G. Bethea, M. W. Focht, T. R. Fullowan, W. A. Gault, K. G. Glogovsky, G. Guth, R. E. Leibenguth, B. F. Levine, G. Lievscu, L. C. Luther, J. W. Stayt, Jr., V. Swaminathan, Y. M. Wong and A. Zussman: Proceedings of the IRIS Specialty Group on Infrared Detectors, **I** (1991) 13.
24 V. Swaminathan, J. W. Stayt, Jr., J. L. Zilko, K. D. C. Trapp, L. E. Smith, S. Nakahara, L. C. Luther, G. Livescu, B. F. Levine, R. E. Leibenguth, K. G. Glogovsky, W. A. Gault, M. W. Focht, C. Buiocchi and M. T. Asom: Proceedings of the IRIS Specialty Group on Infrared Detectors (Moffet Field, CA, USA, 1992).

25 S. D. Gunapala and S. V. Bandara: Semiconductors and Semimetals **62** (Academic Press, 1999) 197-282.

26 S. D. Gunapala, S. V. Bandara, A. Singh, J. K. Liu, S. B. Rafol, E. M. Luong, J. M. Mumolo, N. Q. Tran, J. D. Vincent, C. A. Shott, J. Long and P. D. LeVan: SPIE **3698** (1999) 687.

27 S. V. Bandara, S. D. Gunapala, J. K. Liu, E. M. Luong, J. M. Mumolo, W. Hong, D. K. Sengupta and M. J. McKelvey: Appl. Phys. Lett. **72** (1998) 2427.

28 S. V. Bandara, S. D. Gunapala, J. K. Liu, E. M. Luong, J. M. Mumolo, W. Hong, D. K. Sengupta and M. J. McKelvey: SPIE **3379** (1998) 396.

29 M. Anbar, C. A. Brown, L. Milescu and J. A. Babalola: SPIE **3698** (1999) 93–99.